



UvA-DARE (Digital Academic Repository)

Identification of an X-Ray Pulsar in the BeXRB System IGR J18219-1347

O'Connor, B.; Göğüş, E.; Huppenkothen, D.; Kouveliotou, C.; Gorgone, N.; Townsend, L.J.; Calamida, A.; Fruchter, A.; Buckley, D.A.H.; Baring, M.G.; Kennea, J.A.; Younes, G.; Arzoumanian, Z.; Bellm, E.; Cenko, S.B.; Gendreau, K.; Granot, J.; Hailey, C.; Harrison, F.; Hartmann, D.; Kaper, L.; Kuttyrev, A.; Slane, P.O.; Stern, D.; Troja, E.; van Der Horst, A.J.; Wijers, R.A.M.J.; Woudt, P.

DOI

[10.3847/1538-4357/ac5032](https://doi.org/10.3847/1538-4357/ac5032)

Publication date

2022

Document Version

Final published version

Published in

Astrophysical Journal

License

CC BY

[Link to publication](#)

Citation for published version (APA):

O'Connor, B., Göğüş, E., Huppenkothen, D., Kouveliotou, C., Gorgone, N., Townsend, L. J., Calamida, A., Fruchter, A., Buckley, D. A. H., Baring, M. G., Kennea, J. A., Younes, G., Arzoumanian, Z., Bellm, E., Cenko, S. B., Gendreau, K., Granot, J., Hailey, C., Harrison, F., ... Woudt, P. (2022). Identification of an X-Ray Pulsar in the BeXRB System IGR J18219-1347. *Astrophysical Journal*, 927(2), [139]. <https://doi.org/10.3847/1538-4357/ac5032>

General rights

It is not permitted to download or to forward/distribute the text or part of it without the consent of the author(s) and/or copyright holder(s), other than for strictly personal, individual use, unless the work is under an open content license (like Creative Commons).

Disclaimer/Complaints regulations

If you believe that digital publication of certain material infringes any of your rights or (privacy) interests, please let the Library know, stating your reasons. In case of a legitimate complaint, the Library will make the material inaccessible and/or remove it from the website. Please Ask the Library, <https://uba.uva.nl/en/contact>, or a letter to: Library of the University of Amsterdam, Secretariat, Singel 425, 1012 WP Amsterdam, The Netherlands. You will be contacted as soon as possible.



Identification of an X-Ray Pulsar in the BeXRB System IGR J18219–1347

B. O'Connor^{1,2,3,4} , E. Göğüş⁵ , D. Huppenkothen⁶ , C. Kouveliotou^{1,2} , N. Gorgone^{1,2} , L. J. Townsend⁷ , A. Calamida⁸ , A. Fruchter⁸ , D. A. H. Buckley^{7,9} , M. G. Baring¹⁰ , J. A. Kennea¹¹ , G. Younes^{1,2} , Z. Arzoumanian¹², E. Bellm¹³ , S. B. Cenko^{4,14} , K. Gendreau¹² , J. Granot^{1,15,16} , C. Hailey¹⁷ , F. Harrison¹⁸ , D. Hartmann¹⁹ , L. Kaper²⁰, A. Kutyrav^{3,4} , P. O. Slane²¹ , D. Stern²² , E. Troja^{3,4} , A. J. van der Horst^{1,2} , R. A. M. J. Wijers²³ , and P. Woudt⁹

¹ Department of Physics, The George Washington University, Washington, DC 20052, USA; oonorb@gwmail.gwu.edu

² Astronomy, Physics and Statistics Institute of Sciences (APSiS), The George Washington University, Washington, DC 20052, USA

³ Department of Astronomy, University of Maryland, College Park, MD 20742-4111, USA

⁴ Astrophysics Science Division, NASA Goddard Space Flight Center, 8800 Greenbelt Road, Greenbelt, MD 20771, USA

⁵ Sabanci University, Faculty of Engineering and Natural Sciences, Istanbul 34956, Turkey

⁶ SRON Netherlands Institute for Space Research, Niels Bohrweg 4, 2333CA Leiden, The Netherlands

⁷ South African Astronomical Observatory, P.O. Box 9, 7935 Observatory, South Africa

⁸ Space Telescope Science Institute, 3700 San Martin Drive, Baltimore, MD 21218, USA

⁹ Department of Astronomy, University of Cape Town, Private Bag X3, Rondebosch 7701, South Africa

¹⁰ Department of Physics and Astronomy—MS 108, Rice University, 6100 Main Street, Houston, TX 77251-1892, USA

¹¹ Department of Astronomy and Astrophysics, The Pennsylvania State University, 525 Davey Laboratory, University Park, PA 16802, USA

¹² X-Ray Astrophysics Laboratory, NASA Goddard Space Flight Center, 8800 Greenbelt Road, Greenbelt, MD 20771, USA

¹³ DIRAC Institute, Department of Astronomy, University of Washington, 3910 15th Avenue Northeast, Seattle, WA 98195, USA

¹⁴ Joint Space-Science Institute, University of Maryland, College Park, MD 20742 USA

¹⁵ Department of Natural Sciences, The Open University of Israel, P.O. Box 808, Ra'anana 43537, Israel

¹⁶ Astrophysics Research Center of the Open university (ARCO), The Open University of Israel, P.O. Box 808, Ra'anana 43537, Israel

¹⁷ Columbia Astrophysics Laboratory, Columbia University, New York, NY 10027, USA

¹⁸ Cahill Center for Astrophysics, California Institute of Technology, 1216 East California Boulevard, Pasadena, CA 91125, USA

¹⁹ Department of Physics and Astronomy, Clemson University, Kinard Laboratory of Physics, Clemson, SC 29634-0978, USA

²⁰ University of Amsterdam, Science Park 904, 1098 XH Amsterdam, The Netherlands

²¹ Center for Astrophysics, Harvard & Smithsonian, 60 Garden Street, Cambridge, MA 02138, USA

²² Jet Propulsion Laboratory, California Institute of Technology, 4800 Oak Grove Drive, Mail Stop 169-221, Pasadena, CA 91109, USA

²³ Anton Pannekoek Institute, University of Amsterdam, Postbus 94249, 1090 GE Amsterdam, The Netherlands
Received 2021 November 24; revised 2022 January 21; accepted 2022 January 24; published 2022 March 10

Abstract

We report on observations of the candidate Be/X-ray binary (BeXRB) IGR J18219–1347 with the Swift/X-ray Telescope, the Nuclear Spectroscopic Telescope ARray, and the Neutron Star Interior Composition Explorer during Type-I outbursts in 2020 March and June. Our timing analysis revealed the spin period of a neutron star with $P_{\text{spin}} = 52.46$ s. This periodicity, combined with the known orbital period of 72.4 days, indicates that the system is a BeXRB. Furthermore, by comparing the spectral energy distribution of the infrared counterpart to that of known BeXRBs, we confirm this classification and set a distance of approximately 10–15 kpc for the source. The broadband X-ray spectrum (1.5–50 keV) of the source is described by an absorbed power law with a photon index $\Gamma \sim 0.5$ and a cutoff energy at ~ 13 keV.

Unified Astronomy Thesaurus concepts: X-ray astronomy (1810); High mass x-ray binary stars (733); Pulsars (1306); Neutron stars (1108)

1. Introduction

High-mass X-ray binaries (HMXBs) consist of a compact object (white dwarf, neutron star (NS), or black hole) and a massive ($>10 M_{\odot}$) companion star that donates matter to the compact object. A subclass of HMXBs, known as Be/X-ray binaries (BeXRBs), consists of a compact object with a Be star companion with a decretion disk, which is formed by material ejected from the Be star surface due to its rapid rotation (see Rivinius et al. 2013 for a recent review). Up to $\sim 49\%$ of the HMXB population in the Milky Way consists of BeXRBs (Coleiro & Chaty 2013).

Accretion occurs as the compact object, primarily an NS, which is generally on a wide, highly eccentric orbit, passes

through the decretion disk of the Be companion. During these passages, the system undergoes periodic bright Type-I outbursts (lasting days to weeks; Okazaki & Negueruela 2001; Reig 2007; Chaty 2011). BeXRBs generally exhibit long orbital periods (15–400 days; Reig 2011), which are found to be correlated to the spin period of the compact object (see Corbet diagram; Corbet 1984, 1986). Long-term monitoring is critical to uncover the binary orbital period, and it is confirmed through the repeated detection of Type-I outbursts.

IGR J18219–1347 (hereafter J18219) was discovered with the INTEGRAL satellite in 2010 (Krivonos et al. 2010). An earlier X-ray analysis of Swift/Burst Alert Telescope (BAT) and X-ray Telescope (XRT) data (La Parola et al. 2013) showed that the source X-ray flux exhibited strong variability as a function of its orbit, leading to periodic outbursts. La Parola et al. (2013) associated these with the periastron passage of the compact object, leading to the determination of an orbital period of ~ 72.4 days. Further evidence of the BeXRB nature of

the system was reported by Karasev et al. (2012). Their Chandra localization of the source coincided with a bright infrared (IR) counterpart in the United Kingdom Infrared Telescope (UKIRT) Infrared Deep Sky Survey (UKIDSS; Lawrence et al. 2007); a candidate Be star.

We detected J18219 during our Swift Deep Galactic Plane Survey (DGPS; PI: C. Kouveliotou). We present here new X-ray observations of the source obtained with Swift, the Neutron Star Interior Composition Explorer (NICER), and the Nuclear Spectroscopic Telescope ARray (NuSTAR). We organize the paper as follows. We introduce the observations and data analysis in Section 2. In Section 3 we report on the timing and spectral analyses of our X-ray data and on our search for the optical counterpart of J18219. Finally, we compare the spectral energy distribution (SED) of the candidate IR counterpart to that of known Be stars (Section 3.3). We present a discussion of our results in Section 4 and our conclusions in Section 5.

Unless otherwise stated, confidence intervals or upper limits are presented at the 1σ or 3σ level, respectively. Photometry is reported in the AB magnitude system, except where specified differently.

2. Observations and Data Analysis

We detected J18219 in 2020 March with the Neil Gehrels Swift Observatory (Gehrels et al. 2004) XRT (Burrows et al. 2005) in photon-counting (PC) mode. The source brightness justified triggering our approved target of opportunity (ToO) observation with the NuSTAR (Harrison et al. 2013). We observed the source again in 2020 May to complete the required DGPS 5 ks exposure of the tile. The source brightness indicated a possible outburst, leading to a NICER (Gendreau et al. 2016) director’s discretionary time (DDT) request. Table A1 shows the log of all X-ray observations.

We also performed optical imaging with the Robert Stobie Spectrograph (RSS) on the 11 m Southern African Large Telescope (SALT) and the Large Monolithic Imager (LMI) on the 4.3 m Lowell Discovery Telescope (LDT) to identify and characterize the optical counterpart of J18219 (see Section 2.2). In addition, we analyzed archival UKIDSS IR imaging.

2.1. X-Ray Observations

2.1.1. Swift/BAT

J18219 is one of the long-term monitoring targets with the Swift/BAT (Barthelmy et al. 2005). All target data are daily averaged in the 15–50 keV energy band and stored at the Swift/BAT Hard X-ray Transient Monitor archive²⁴ (Krimm et al. 2013). We analyzed data spanning 3369 days (MJD 55968–59337) to refine the orbital period previously identified by La Parola et al. (2013; see Section 3.1). The data were not barycenter corrected; the significantly long orbital period (72.4 days) renders the correction effect negligible.

2.1.2. Swift/XRT

Swift/XRT observations of J18219 comprise 22 epochs, totaling 49.4 ks, with 29.8 ks in windowed timing (WT) mode and 19.6 ks in PC mode. The WT mode data comprise largely the observing campaign requested by Krimm et al. (2012) and

reported by La Parola et al. (2013; see Table A1). In this work we analyze all WT data together with the PC mode observations (ObsIDs: 3110746, 3110747, and 3110855) obtained through the DGPS.

We reduced and analyzed the PC mode observations using standard filtering and cleaning procedures in the `xrtpipeline` software. The source count rates were determined using the `ximage` routine `sosta` within `HEASOFT v6.27.2`. We used source extraction regions corresponding to an 87% enclosed-energy fraction, and local background annuli surrounding these regions. We then corrected the count rates for vignetting, bad pixels or columns on the CCD, and point-spread function (PSF) losses, using the `xrtmkarf` command combined with the exposure map to recover the full 100% of the enclosed-energy fraction.

Finally, we used the Swift/XRT data products generator²⁵ to obtain the most accurate source position based on all PC mode exposures. The XRT enhanced position (Evans et al. 2009) is R. A., decl. (J2000) = $18^{\text{h}}21^{\text{m}}54^{\text{s}}.92$, $-13^{\circ}47'23''.3$ with an accuracy of $3''.5$ (90% confidence level; hereafter CL). This is consistent with the Chandra localization reported by Karasev et al. (2012): R.A., decl. (J2000) = $18^{\text{h}}21^{\text{m}}54^{\text{s}}.821$, $-13^{\circ}47'26''.703$ with uncertainty $0''.9$ (90% CL).

2.1.3. NuSTAR

We used one of our NuSTAR ToOs to observe J18219 on 2020 March 15 for 23 ks (ObsID: 90601309002). NuSTAR comprises two identical focal plane modules, FPMA and FPMB, covering 3–79 keV. The data reduction was performed using the NuSTAR Data Analysis Software pipeline (NuSTAR-DAS) v1.9.2 and the calibration files (CALDB) version 20200726 within `HEASOFT v6.27.2`. The data were processed using `nupipeline`, and then light curves and spectra were extracted using `nuproducts`. Source spectra were extracted from a $100''$ radius region centered on the transient. The background was similarly extracted from a $100''$ radius source-free region. For our spectral analysis we truncated the NuSTAR data at 50 keV, where the background began to dominate; the spectra were grouped to a minimum of 25 counts per bin for statistical significance. The photon arrival times were barycenter-corrected to the solar system using the `barycorr`²⁶ tool and the latest clockfile.²⁷

We note that in FPMB, the source position is partially contaminated by stray light from the bright low-mass X-ray binary GX 17+2 (Grefenstette et al. 2021). We therefore chose to perform the majority of our analysis using the uncontaminated FPMA data. For the FPMB data, we carefully selected the background region to subtract and minimize the effects of the stray light; in all these cases, we confirmed that including FPMB data did not change our results.

2.1.4. NICER

We observed J18219 with NICER on 2020 June 3 for 2.3 ks (ObsID: 3201610101) through a DDT request. The data were processed using `NICERDAS v7a` within `HEASOFT v6.27.2` and filtered using standard cleaning criteria with `nicerl2`. The cleaned event file was barycenter-corrected (using

²⁵ https://www.swift.ac.uk/user_objects/

²⁶ <https://heasarc.gsfc.nasa.gov/ftools/caldb/help/barycorr.html>

²⁷ `nuClock20100101v116.fits.gz`, see https://nustarsoc.caltech.edu/NuSTAR_Public/NuSTAROperationSite/clockfile.php.

²⁴ <https://swift.gsfc.nasa.gov/results/transients/weak/SWIFTJ1821.8-1348/>

barycorr) to the solar system based on the Chandra position. We then used the `xselect` task to extract the light curve and spectrum between 1 and 10 keV. The NICER background spectrum was estimated using the `nibackgen3C50 v6` tool (Remillard et al. 2022); it dominates at $\lesssim 1.5$ keV. We therefore exclude these energies from our spectral analysis. Finally, the spectra were grouped to a minimum of 25 counts per bin using `grppha`.

We carried out additional NICER DDT observations on 2021 May 2 for 1.2 ks (ObsID: 4201610101). The source was not detected, and we adopt a 3σ upper limit (0.4–12 keV) of ~ 1.2 cts s^{-1} (Remillard et al. 2022), which corresponded to an unabsorbed flux $\lesssim 1.5 \times 10^{-11}$ erg cm^2 s^{-1} for the best-fit model spectrum.

2.2. Optical Imaging

2.2.1. Southern African Large Telescope (SALT)

We carried out optical imaging with the RSS (Burgh et al. 2003; Kobulnicky et al. 2003; Smith et al. 2006) mounted on the 11 m SALT (Buckley et al. 2006) on 2021 June 6. The observations were performed with a clear, fused silica filter for a total exposure time of 720 s. The data were processed by an automated SALT pipeline. We corrected the astrometry using the `astrometry.net` software (Lang et al. 2010). The seeing during these observations was very poor, and no optical counterpart was identified at the Chandra localization in the stacked image. The 3σ upper limit of the image is ~ 22.5 AB mag.

2.2.2. Lowell Discovery Telescope (LDT)

We performed optical observations with the LMI mounted on the 4.3 m LDT (formerly the Discovery Channel Telescope) in Happy Jack, AZ on 2021 August 6 in the i and z filters for a total exposure of 1650 and 1000 s, respectively. The observations were performed under clear observing conditions with seeing $\sim 1''.25$. The median airmass of the observations was ~ 1.5 .

The data were reduced and analyzed using a custom pipeline (Toy et al. 2016) that makes use of standard CCD reduction techniques in the `IRAF`²⁸ package. We used `SCAMP` (Bertin 2006) to align the individual frames, and then `SWarp` (Bertin 2010) to combine the images. The absolute astrometry was calibrated against the Panoramic Survey Telescope and Rapid Response System (Pan-STARRS, hereafter PS1; Chambers et al. 2016; Flewelling et al. 2020) catalog. At the Chandra source position, we do not detect the optical counterpart in either filter. The photometry was computed using the `SExtractor` (Bertin & Arnouts 1996) package, and was calibrated against stars in the PS1 catalog. We obtained upper limits $i \gtrsim 23.7$ and $z \gtrsim 22.1$ AB mag at the source position (not corrected for Galactic extinction; see Table 1).

2.2.3. Pan-STARRS

We searched archival observations²⁹ from PS1 (Chambers et al. 2016; Flewelling et al. 2020) for the optical counterpart to

²⁸ `IRAF` is distributed by the National Optical Astronomy Observatory, which is operated by the Association of Universities for Research in Astronomy (AURA) under cooperative agreement with the National Science Foundation (NSF).

²⁹ <https://ps1images.stsci.edu/cgi-bin/ps1cutouts>

Table 1
Photometry of the Optical/IR Counterparts (Stars A and B) of J18219

Source	Filter	m_λ (mag)		A_λ (mag)
		Star A	Star B	
PS1	g	>22.4	>22.4	29.05
ZTF	g	>22.0	>22.0	30.25
PS1	r	>22.4	>22.4	20.80
ZTF	r	>22.5	>22.5	20.92
PS1	i	>22.3	>22.3	15.41
ZTF	i	>20.9	>20.9	15.55
LDT	i	>23.7	>23.7	15.55
PS1	z	>21.5	>21.5	12.11
LDT	z	>22.1	>22.1	11.57
PS1	y	>20.5	>20.5	9.96
UKIDSS	J	21.3 ± 0.4	18.81 ± 0.05	6.49
UKIDSS	H	18.62 ± 0.07	17.35 ± 0.08	4.11
UKIDSS	K	16.93 ± 0.03	17.35 ± 0.03	2.77
GLIMPSE	$3.6 \mu\text{m}$	15.72 ± 0.07	...	1.63
GLIMPSE	$4.5 \mu\text{m}$	15.60 ± 0.08	...	1.35
GLIMPSE	$5.8 \mu\text{m}$	15.62 ± 0.15	...	1.19

Note. The photometry m_λ is not corrected for Galactic extinction A_λ due to interstellar reddening $E(B - V) = 9.16$ mag (Schlafly & Finkbeiner 2011) in the direction of the source. The magnitudes m_λ are reported in the AB magnitude system.

J18219. At the Chandra position, we do not identify an optical source in any filter. We derive 3σ upper limits in the g , r , i , z , and y -bands. This photometry is reported in Table 1.

2.2.4. Zwicky Transient Facility (ZTF)

We analyzed public archival observations obtained with ZTF (Bellm et al. 2019; Graham et al. 2019) between 2018 March and 2021 June. The data were retrieved from The ZTF Image Service³⁰ (Masci et al. 2019). We used `SWarp` to coadd all the individual science frames, each with an exposure time of 30 s, covering the position of J18219 in g and r band. This resulted in a total exposure of 3150 s (105 frames) and 8160 s (272 frames) in g and r , respectively. In the i band, due to the lack of publicly available observations, we make use of the reference image provided by ZTF, which comprises 15 stacked frames for a total of 450 s exposure. At the position of the IR counterpart, we do not detect a source to a depth $g \gtrsim 22.0$, $r \gtrsim 22.5$, and $i \gtrsim 20.9$ AB mag (3σ). These limits are reported in Table 1 and are consistent with those derived from the PS1 (see Section 2.2.3) and LDT imaging (Section 2.2.2).

2.2.5. UKIDSS

We analyzed public archival observations from UKIDSS (DR11; Lawrence et al. 2007) obtained in the JHK filters with the Wide Field Camera (WFCAM; Casali et al. 2007) mounted on the 3.8 m UKIRT. We downloaded the calibrated images from the WFCAM science archive (Hambly et al. 2008), which showed that the immediate field surrounding J18219 is relatively sparse (Figure 1). We identified in these images the IR counterpart of J18219 proposed by Karasev et al. (2012). Despite the good seeing ($\sim 0''.6$ – $0''.7$), this source appeared to be the blended combination of two point sources, specifically in

³⁰ <https://irsa.ipac.caltech.edu/Missions/ztf.html>

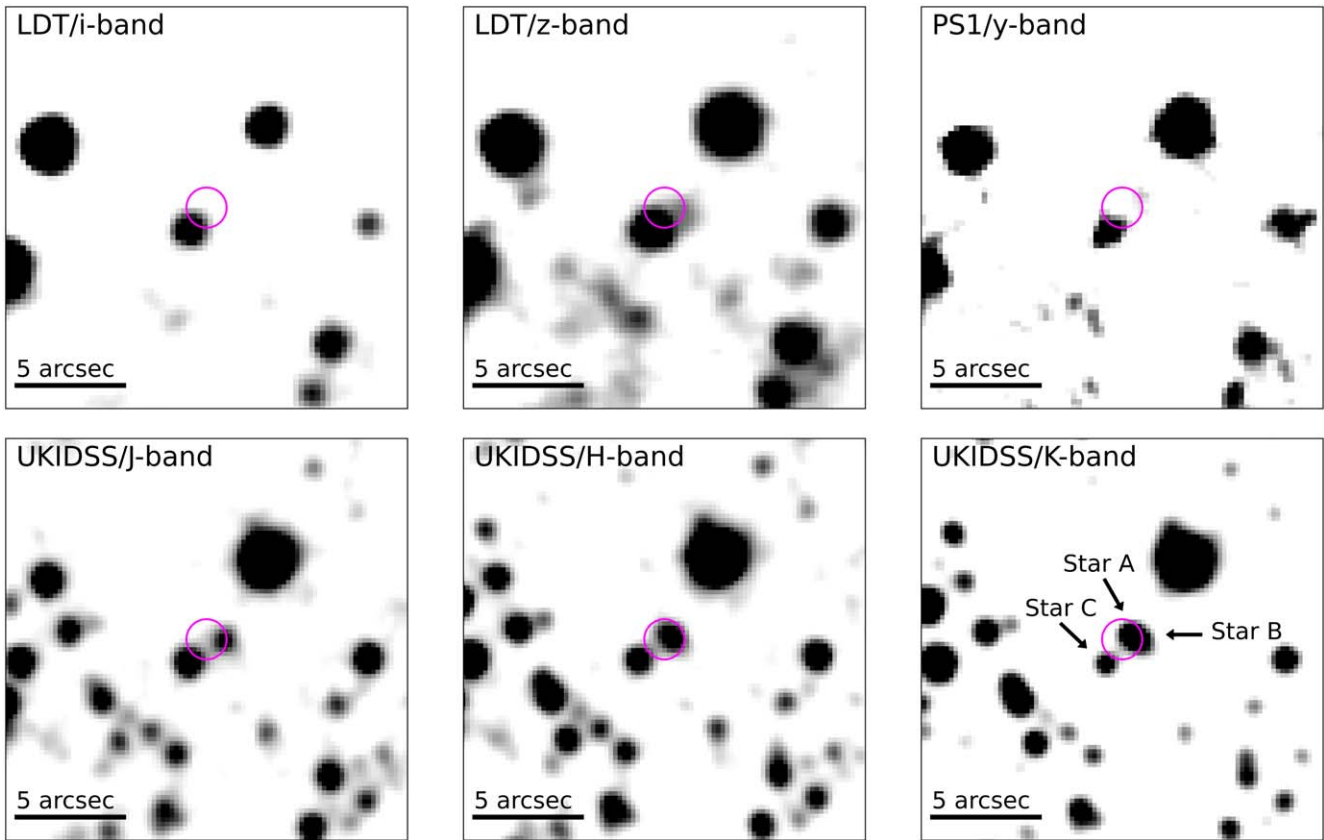


Figure 1. The field of J18219 from our LDT imaging and archival observations from PS1 and UKIDSS. The Chandra/HRC-I localization of the X-ray counterpart (Karasev et al. 2012) is displayed by a magenta circle with a radius $0''.9$ (90% CL). The position of the blended optical counterpart (stars A and B) and the nearby star C are labeled only in the UKIDSS/*K*-band figure (bottom right). Star A is the left star in the star A/B complex. In each figure, north is up and east is to the left. The images are smoothed for display purposes.

the *H* and *K* filters, thus prohibiting the identification of the true counterpart.

To deblend the photometry and resolve the individual sources, referred to as star A and star B, we first performed PSF photometry with DAOPHOT IV/ALLSTAR (Stetson 1987). We also identified another star, referred to as star C, which lies just outside the Chandra localization (90% CL) and might therefore also be considered a potential counterpart.

Next, we generated a photometric catalog for each of the three images (one per filter): the sources were identified in the *K*-band image. We used this image to create a list of objects in the field of view and performed forced photometry on all images with ALLFRAME (Stetson 1994) by using the previously calculated PSFs. These are Moffat functions with a quadratic spatial variation in the field. In order to improve the sky background estimate and the signal-to-noise ratio (S/N), we recalculated the PSF for each image by using the output ALLFRAME catalogs and repeated the forced photometry. To calibrate the photometry to the Vega system, we normalized for exposure time, calculated an aperture correction, and used the zeropoints provided by CASU.³¹ The final catalog includes a total of 4172 stars, 3067 of which have a measurement in *JHK*; it reaches $S/N \approx 5$ at $K \approx 18.5$ Vega mag (20.4 AB mag).

Finally, we converted the photometry from the Vega into the AB magnitude system by using the definition in Hewett et al. (2006). The final calibrated photometry for stars A and B is tabulated in Table 1. We discuss these results in Section 3.3.

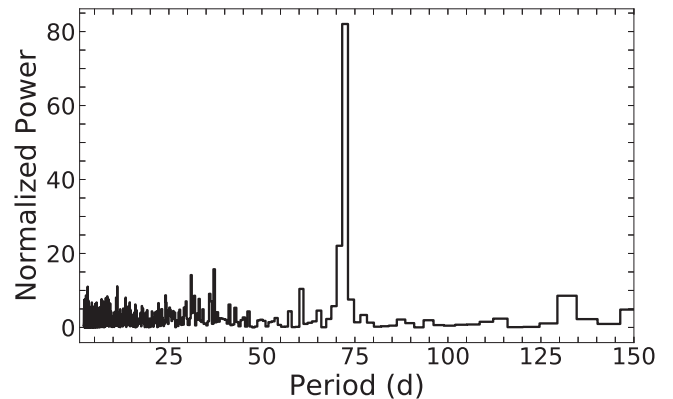


Figure 2. Lomb–Scargle periodogram of the 9.2 yr of Swift/BAT monitoring. The peak corresponds to an orbital period at $P_{\text{orb}} = 72.3 \pm 0.3$ days.

3. Results

3.1. Timing Analysis

3.1.1. Orbital Period

We used the long-term Swift/BAT monitoring data (see Section 2.1.1) to search for a periodic signal, as previously reported by La Parola et al. (2013). A Lomb–Scargle frequency analysis (Scargle 1982) revealed an orbital period at $P_{\text{orb}} = 72.3 \pm 0.3$ days (see Figure 2), consistent with the period (72.4 ± 0.3 days) derived by La Parola et al. (2013). We calculate a false-alarm probability of 2×10^{-31} (Baluev 2008).

³¹ <http://casu.ast.cam.ac.uk/surveys-projects/wfcam/technical/photometry>

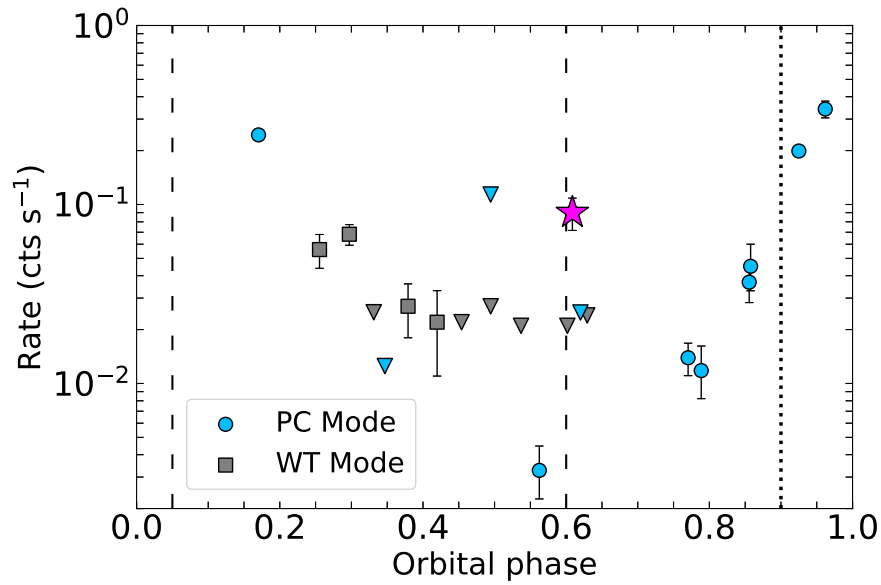


Figure 3. Swift/XRT observations of J18219 as a function of orbital phase. Data in PC (WT) mode are shown with blue circles (gray squares); 3σ upper limits are denoted by downward triangles. The magenta star (PC mode data) represents a significant outlier—an outburst occurring close to apastron on MJD 58177. Dashed (dotted) vertical lines represent the orbital phase of our NICER (NuSTAR) observations.

Our analysis covers ~ 9.2 yr (corresponding to ~ 45 orbits) of BAT observations, confirming the orbital period of the system. Throughout this work, we define the orbital phase with respect to MJD 54656.26 assuming a period $P_{\text{orb}} \approx 72.4$ days for comparison with La Parola et al. (2013). However, here we define the orbital phase of periastron passage as 0.0 phase, whereas in La Parola et al. (2013) the periastron passage (peak of the BAT epoch-folded light curve) occurs at 0.51 phase. In Table A1 we report the orbital phase of all X-ray observations used in this work.

Figure 3 displays the Swift/XRT PC and WT mode observations as a function of orbital phase. We observe a clear trend of the source brightening and fading over the course of its orbit as it approaches and departs periastron passage. However, we also note the presence of a single X-ray detection occurring very close to apastron on MJD 58177, shown by the magenta star. At the same time, several observations at a similar orbital phase (~ 0.6) to the magenta point resulted in upper limits, which leads us to conclude that this source behavior is uncommon. If such an outburst were to occur at apastron in every cycle, the source brightness would have to increase by a factor of $\gtrsim 4$ within 0.5 day based on our upper limits and would have to decrease again by the same factor within 0.8 day.

To further explore this scenario, we observed the source with NICER at phase ~ 0.6 ; the source was not detected with an upper limit to the unabsorbed flux of $< 1.5 \times 10^{-11}$ erg cm^{-2} s^{-1} (0.4–12 keV). Our NICER (2021 May; Table A1) observation would have been sensitive to an outburst similar to that observed on MJD 58177, which had an estimated unabsorbed flux $\sim 3 \times 10^{-11}$ erg cm^{-2} s^{-1} (0.3–10 keV), assuming the best-fit model spectrum (see Section 3.2.1 and Table 2). Finally, a search in the daily BAT light curve (15–50 keV) around MJD 58177 did not reveal significant evidence for an outburst (15–50 keV). We briefly discuss this apastron X-ray flux excess in Section 4.

Table 2
Time-averaged and Time-resolved Spectral Analysis Results of J18219 X-Ray Observations Using an Absorbed Cutoff Power-law (`tbabs*cutoffpl`)

Time-averaged	NICER ^a	NuSTAR	NuSTAR and NICER
N_{H} (10^{22} cm^{-2})	7.4 ± 0.4	11.2 ± 0.8	8.3 ± 0.3
Γ	0.37 ± 0.07	0.65 ± 0.04	0.51 ± 0.03
E_{cut} (keV)	14 (frozen)	14.7 ± 0.6	13.3 ± 0.04
N_{FPMA}	...	1.0	1.0
N_{FPMB}	...	0.97 ± 0.01	0.94 ± 0.02
N_{NICER}	1.0	...	0.87 ± 0.02
F_{X}^{b} (10^{-10} erg cm^{-2} s^{-1})	0.67 ± 0.012	1.93 ± 0.02	1.37 ± 0.02
Cstat	734 (685 dof)	1377 (1245 dof)	2130 (1929 dof)
NuSTAR time-resolved	<i>Decreasing</i>	<i>Increasing</i>	<i>Linked N_{H} and E_{cut}</i>
N_{H} (10^{22} cm^{-2})	10.1 ± 1.8	12.5 ± 1.9	10.4 ± 1.3
Γ	0.70 ± 0.10	0.72 ± 0.10	0.67 ± 0.07
Γ_2^{c}	0.70 ± 0.07
E_{cut} (keV)	16.3 ± 1.7	16.9 ± 1.9	16.7 ± 1.3
N_{FPMA}	1.0	1.0	1.0
N_{FPMB}	0.94 ± 0.01	0.95 ± 0.01	0.94 ± 0.01
F_{X} (10^{-10} erg cm^{-2} s^{-1})	2.12 ± 0.07	1.93 ± 0.07	1.98 ± 0.04
$F_{\text{X},2}^{\text{c}}$ (10^{-10} erg cm^{-2} s^{-1})	2.25 ± 0.06
Cstat	652 (682 dof)	604 (653 dof)	1330 (1335 dof)

Notes.

^a The NICER-only model flux is provided in the 2–10 keV energy range.

^b Unabsorbed flux (3–50 keV).

^c Decreasing state only.

3.1.2. Spin Period

We searched the NuSTAR (2020 March) and NICER (2020 June; Table A1) data for coherent pulsations using both Z^2

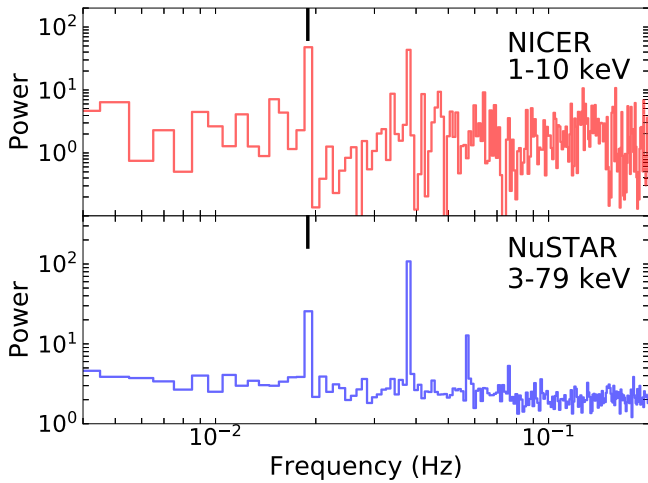


Figure 4. Leahy normalized periodogram for our NICER (1–10 keV; top) and NuSTAR (3–79 keV; bottom) observations. The spin frequency (marked by the vertical black line) is found at 0.019 Hz, corresponding to a period of 52.46 s. A number of harmonics of this frequency are also observed at 0.038, 0.057, and 0.076 Hz.

statistics (Buccheri et al. 1983) and by building the Leahy normalized power spectral density (PSD). The Leahy normalized periodogram (Leahy et al. 1983) for these observations, computed using *Stingray* (Huppenkothen et al. 2019), is shown in Figure 4. The periodogram was built from the NuSTAR and NICER light curves with events binned in time intervals of $\delta t = 2$ s, and averaged over segments with duration of $\tau = 10^3$ s. Therefore, the NuSTAR periodogram is averaged over 46 segments (including both FPMA/B), whereas NICER is averaged over only 2 segments due to the shorter exposure, using the *AveragedPowerspectrum* task within *Stingray*.

We identify strong pulsations in NuSTAR at the frequency of 0.0190593(1) Hz. This corresponds to a period $P_{\text{spin}} = 52.4680 \pm 0.0003$ s, which we interpret as the spin period of an NS in the binary system. NICER observations ~ 80 days later also show a coherent signal at 0.01906(1) Hz, yielding a period of 52.466 ± 0.007 s. The two spin frequencies are consistent with each other within 1σ .

In addition, we observe a number of harmonics of the spin frequency in the PSD at 0.038 Hz in NICER, and 0.038, 0.057, and 0.076 Hz in NuSTAR (Figure 4), corresponding to $n = 2, 3,$ and 4 in the Fourier series decomposition, which are all detected at a $>3\sigma$ CL. We note that the most significant peak in the NuSTAR Leahy normalized periodogram is located at 0.0381185(2) Hz, but we disregard this as the fundamental frequency due to the presence of the peak at 0.057 Hz, which is not an expected harmonic of 0.038 Hz. We also note that using Z_n^2 epoch-folding statistics (Buccheri et al. 1983), where n is the number of harmonics, leads to a higher significance peak at 0.019 Hz when $n = 2$ and 3 (i.e., Z_3^2) as the pulse profile is not strictly sinusoidal (i.e., $n = 1$, which favors 0.038 Hz).

We additionally searched for a similar timing feature in our Swift/XRT PC mode data and our NICER observation from 2021 May, but due to the low number of counts, we were unable to find a significant peak at the expected frequency.

In Figures 5 and 6 we present the pulse profiles for NuSTAR and NICER (2020 June observation) in several energy bands. In NuSTAR, a well-defined pulse profile is detected in all energy bands, whereas in NICER, the pulsations are very weak in the 1–3 keV band (due to the high NICER background below 1.5 keV), but increase in strength above 3 keV. The

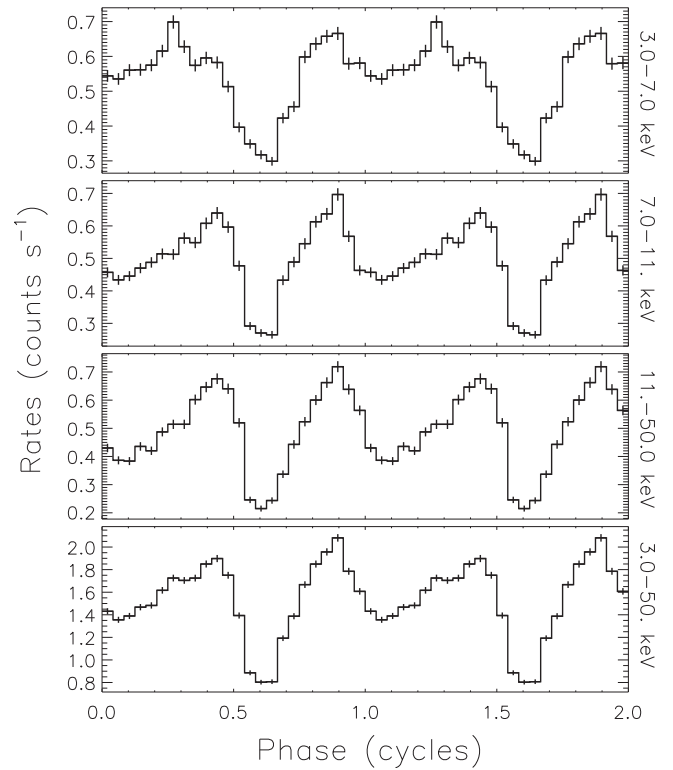


Figure 5. Phase-folded light curve from our NuSTAR (FPMA/B) observation.

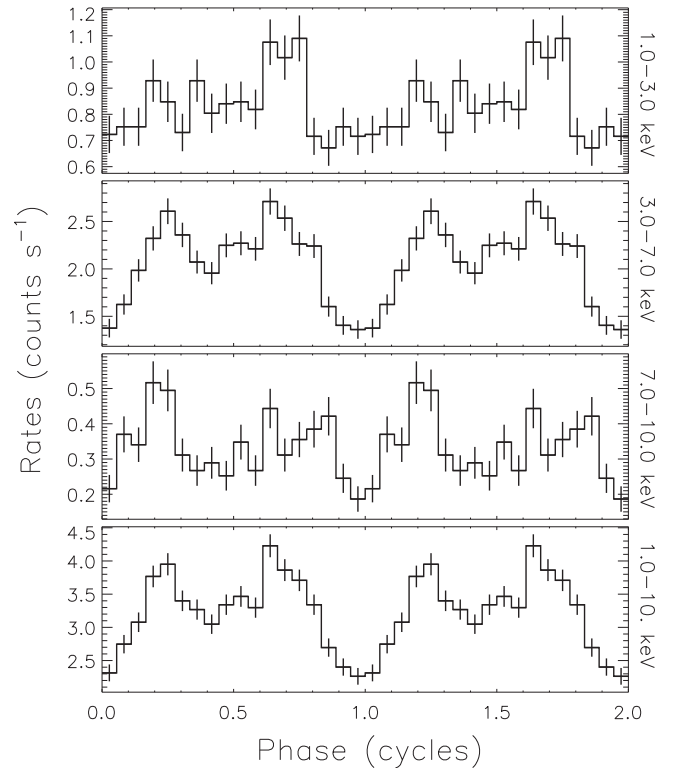


Figure 6. Phase-folded light curve from our NICER observation on 2020 June.

phase-folded profiles display a similar shape at the common energy bands (i.e., 3–7 keV) in NuSTAR and NICER. The two peaks in both phase-folded light curves are separated by ~ 0.5 phase, which in combination with their similar peak heights drives the appearance of the harmonics in the periodogram.

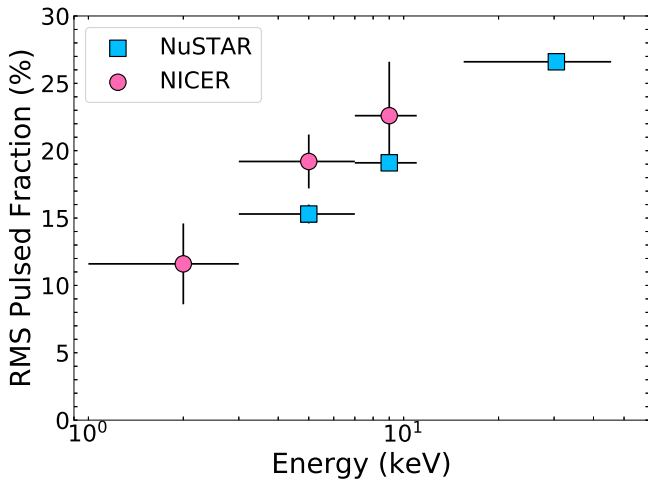


Figure 7. The rms pulsed fraction as a function of energy for our NuSTAR and NICER (2020 June) observations.

We computed the root mean square (rms) pulsed fraction in these energy bands for both instruments using the definition from Dhillon et al. (2009; their Equation (2)). We observe a clear trend in the rms pulsed fraction: it increases from $\sim 20\%$ in the soft (3–7 keV) band to $\sim 28\%$ in the harder (11–50 keV) band, as displayed in Figure 7. This trend of increasing pulsed fraction with energy is commonly observed in X-ray pulsars within HMXB systems (Lutovinov & Tsygankov 2008). The pulsed fraction in the full band for each instrument is $22.0\% \pm 0.3\%$ for NuSTAR (3–50 keV) and $16.5\% \pm 1\%$ for NICER (1–10 keV).

3.1.3. NuSTAR Light Curve Variability

In Figure 8 we show the NuSTAR/FPMA light curve in the 3–6, 6–10, and 10–50 keV energy ranges. The light curve displays variability on a timescale of ~ 5000 – 6000 s. To explore whether this is identified as a timing feature, we again used *Stingray* to build the Leahy normalized periodogram, instead using the *Powerspectrum* task with the light curve binned in time intervals of $\delta t = 100$ s. The orbital gaps in the light curve were filled with white noise to minimize the effect of NuSTAR’s low-Earth orbit duration (~ 5800 s) on the periodogram. This analysis was performed for both the FPMA and FPMB light curves individually, as well as for the combined FPMA/B light curve. We did not identify either a coherent or quasi-periodic oscillation on the timescale of the observed light curve variability (~ 5000 – 6000 s). In fact, the power spectrum was found to be consistent with stochastic (red) noise (Press 1978).

The light curve variability is visible across all energies (3–6, 6–10, and 10–50 keV) with a consistent trend between the different energy bands (Figure 8). To probe the nature of this variability, we further explore the spectral variability of the source over these timescales in Section 3.2.2.

3.2. Spectral Analysis

3.2.1. Time-averaged Spectroscopy

We performed a time-averaged spectral analysis of the NuSTAR observation in the 3–50 keV energy band using XSPEC v12.11.0 (Arnaud 1996). Both the FPMA and FPMB

spectra were fit simultaneously with a prefactor. The normalization of FPMA N_{FPMA} was fixed to unity, and we allowed the normalization of FPMB N_{FPMB} to vary. The prefactor N_{FPMB} varied by $\lesssim 10\%$ compared to unity, likely due to a rip in the multilayer insulation of FPMB (see Madsen et al. 2020). We fit the spectra with an absorbed cutoff power law (model `con*tbabs*cutoffpl`) with the interstellar matter abundance table set using the command `abund wilm` (Wilms et al. 2000). This resulted in a good spectral fit ($C_{\text{stat}} = 1377$ for 1245 degrees of freedom, hereafter dof; Cash 1979). We then used the `cflux` model to derive the time-averaged unabsorbed flux for the model.

Finally, we tested an absorbed power-law model, which provided a much worse fit of the data ($C_{\text{stat}} = 2154$ for 1246 dof). We therefore consider the absorbed cutoff power law to be the best-fit model for the time-averaged flux and report its parameter values in Table 2.

We next fit the spectrum of our NICER observations also with an absorbed cutoff power law (1.5–10 keV). Due to the narrower spectral range of NICER, the cutoff power-law model did not provide a meaningful constraint on the cutoff energy. Therefore, we fixed the cutoff energy to 14 keV, in agreement with the value derived in our NuSTAR spectrum (14.7 ± 0.6 keV). The results of this analysis are also presented in Table 2.

Our NuSTAR and NICER observations were obtained in a similar orbital phase: NuSTAR at phase ~ 0.9 and NICER at phase ~ 0.01 (see Figure 9). We therefore expected that the NS interaction with the Be decretion disk would be similar in both observations. We therefore performed an additional joint fit, including both NuSTAR and NICER spectra, using an absorbed cutoff power-law model. We allowed the normalization of the NICER spectrum to vary with respect to the normalization of NuSTAR/FPMA, yielding a value of ~ 0.87 . The results of this analysis are included in Table 2, and the fit residuals are displayed in the bottom panel of Figure 10. In addition, we tested a joint fit including the combined NuSTAR, NICER, and Swift/XRT PC mode spectra, and obtained the same result as in Table 2 (NuSTAR and NICER column) with no variation in the fit parameters or their errors.

Our time-averaged spectral results are consistent with the combined Swift/XRT and Swift/BAT spectral analysis presented in La Parola et al. (2013), albeit with smaller uncertainty on the fit parameters. We do note, however, that the N_{H} inferred by La Parola et al. (2013) of $4.3_{-1.7}^{+3.8} \times 10^{22} \text{ cm}^{-2}$ is smaller, but consistent at the 2σ level with our value. Both N_{H} values are in excess of the Galactic value, $N_{\text{H,gal}} = 1.49 \times 10^{22} \text{ cm}^{-2}$ (Willingale et al. 2013), implying a potentially significant contribution intrinsic to the source environment. We tested whether this excess N_{H} was required by performing a joint NuSTAR and NICER fit with fixed $N_{\text{H}} = 1.49 \times 10^{22} \text{ cm}^{-2}$. This resulted in a very poor fit to the data ($C_{\text{stat}} = 3478$ for 1929 dof) with significant residuals compared to the best-fit model ($C_{\text{stat}} = 2130$ for 1929 dof).

The phenomenological cutoff power-law model suggests a physical emission mechanism of thermal inverse Compton scattering (Titarchuk 1994). We therefore fit the broadband X-ray spectrum (NuSTAR and NICER) with a thermally Comptonized model `CompTT` in XSPEC (`con*tbabs*CompTT`; Titarchuk 1994). The analytical `CompTT` model is described by the temperature of soft X-ray seed photons of

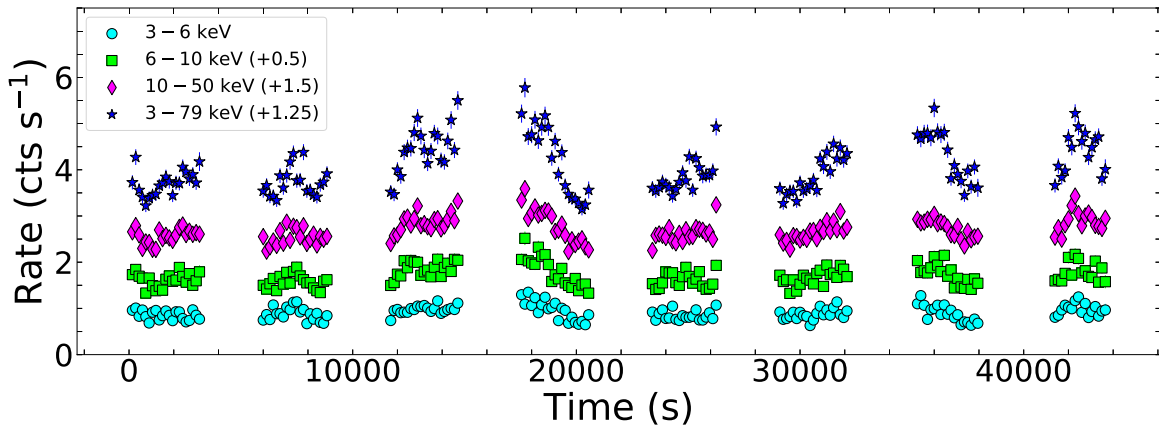


Figure 8. NuSTAR/FPMA light curve of J18219 in the 3–6, 6–10, 10–50, and 3–79 keV energy range with a time bin of 110 s. The 6–10, 10–50, and 3–79 keV light curves have been shifted upward by 0.5, 1.5, and 1.25 cts s^{-1} , respectively.

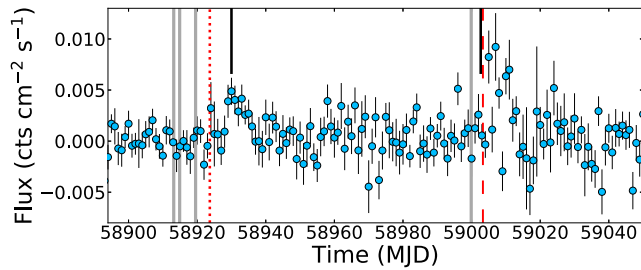


Figure 9. Swift/BAT light curve including our NuSTAR and NICER observations in 2020 March and June (dotted and dashed red lines, respectively). Solid black lines mark the expected periastron passage of the NS, and solid gray lines mark our Swift/XRT observations.

Table 3
Results for a Joint NuSTAR and NICER Spectral Fit with a Thermally Comptonized (CompTT) Model

Parameter	Value	Units
N_{H}	4.79 ± 0.25	10^{22} cm^{-2}
kT_0	1.36 ± 0.03	keV
kT_1	6.98 ± 0.13	keV
τ	5.19 ± 0.11	
N_{FPMA}	1.0	
N_{FPMB}	0.88 ± 0.01	
N_{NICER}	0.86 ± 0.02	
$F_{\text{X}}(3-50 \text{ keV})$	1.26 ± 0.04	$10^{-10} \text{ erg cm}^{-2} \text{ s}^{-1}$
Cstat	2079 (1928 dof)	

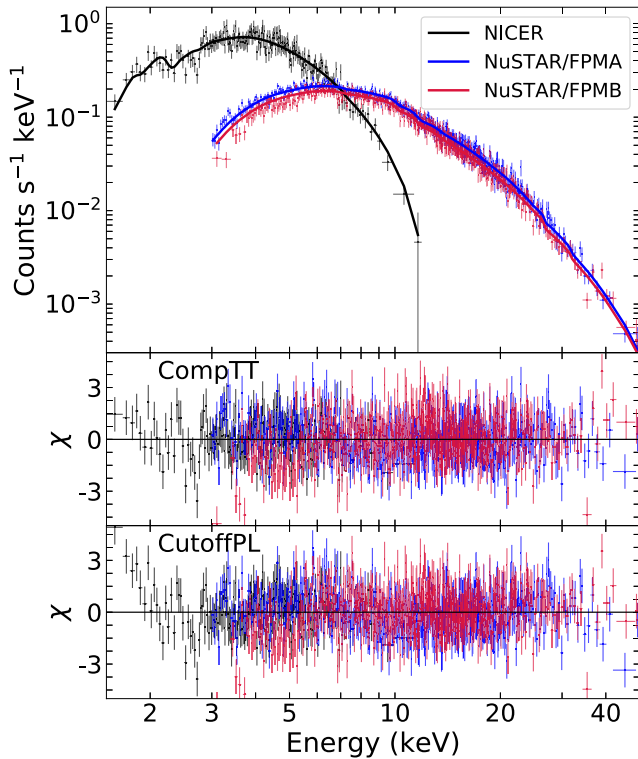


Figure 10. Joint NuSTAR and NICER fit (1.5–50 keV). The combined spectrum is well described by a thermally Comptonized model (top panel). The middle panel displays the fit residuals for the CompTT model, whereas the bottom panel shows the residuals for the absorbed cutoff power-law model.

temperature kT_0 , which are Comptonized by a hot plasma with temperature kT_1 and optical depth τ . We find that this model provides an improved description of the low-energy (<2 keV) emission observed in NICER with smaller residuals (Cstat = 2079 for 1928 dof; see Figure 10). The best-fit model (Table 3) has $kT_0 = 1.36 \pm 0.03$ keV and $kT_1 = 6.98 \pm 0.13$ keV with an optical depth $\tau = 5.19 \pm 0.11$. The fit also resulted in a smaller hydrogen column density of $N_{\text{H}} = (4.79 \pm 0.25) \times 10^{22} \text{ cm}^{-2}$ compared to that implied by the phenomenological cutoff power-law model.

3.2.2. Time-resolved Spectroscopy

In this section, we investigate whether spectral variability can explain the flux variability observed with NuSTAR on a scale of a few thousand seconds (Figure 8). We split the NuSTAR light curve (FPMA and FPMB) into two groups: intervals of the light curve that are either increasing or decreasing in count rate. These intervals were selected based on the 3–79 keV light curve displayed in Figure 8. In the event that the light curve obtained over an individual NuSTAR orbit displays variability (i.e., a switch from increasing to decreasing, or vice versa), the increasing and decreasing intervals were chosen to reflect this variability such that only increasing portions of the light curve are included in the increasing spectral analysis. We note that some small portions of the light curve are not strictly increasing or decreasing, and therefore, these portions were ignored in our analysis. We used XSELECT to define good time intervals (GTIs) and to extract the spectra, which were then binned to a minimum of 25 counts per

Table 4
Phase-resolved Spectral Analysis Results of Our NuSTAR (FPMA/B) Observations

NuSTAR Phase-resolved	<i>Shoulder</i>	<i>Small Peak</i>	<i>Valley</i>	<i>Main Peak</i>
<i>Phase</i> ^a	0.0–0.25	0.25–0.5	0.5–0.75	0.75–1.0
N_{H} (10^{22} cm ⁻²)	$5.8 \pm 0.5^{\text{b}}$
Γ	0.82 ± 0.04	0.56 ± 0.04	0.69 ± 0.05	0.56 ± 0.05
E_{cut} (keV)	$14.5 \pm 0.6^{\text{b}}$
N_{FPMA}	1.0^{b}
N_{FPMB}	$1.08 \pm 0.01^{\text{b}}$
A_{norm} (10^{-3})	4.0 ± 0.3	2.7 ± 0.2	2.8 ± 0.2	2.2 ± 0.2
Cstat	478 (469 dof)	530 (560 dof)	357 (347)	569 (568 dof)

Notes.

^a Phase selection is based on Figure 5.

^b The hydrogen column density, cutoff energy, and the normalization of FPMA/B were fixed among the four phase-resolved spectra.

bin; we used the Cash statistic within XSPEC for the model fitting. We modeled the spectra with the phenomenological absorbed cutoff power law as outlined in Section 3.2.1. We chose to apply this model, as opposed to CompTT, due to its smaller number of fit parameters.

We find that the increasing and decreasing states can be described by the same spectrum (absorbed cutoff power law) within 1σ errors. In order to more precisely determine the normalization and photon index, we linked the hydrogen column density and cutoff energy within XSPEC, requiring these parameters to be identical for both spectra. The results of these analyses are presented in Table 2. We conclude that spectral variability cannot explain the observed flux modulation.

3.2.3. Phase-resolved Spectroscopy

We performed a phase-resolved spectral analysis with the NuSTAR FPMA/B data to determine if there is spectral variability over the NS spin period. We selected the GTIs following the NuSTAR phase-folded light curve displayed in Figure 5. Based on the double-peaked pulse profile, we selected four spectral groups: (i) the shoulder of the small peak (phase 0.0–0.25), (ii) the small peak between phase 0.25–0.5, (iii) the valley between phase 0.5–0.75, and last, (iv) the main peak at 0.75–1.0 phase. These spectra were modeled using an absorbed cutoff power law as in the previous section.

The hydrogen column density, photon index, and cutoff energy were consistent within the $1-2\sigma$ level among the four phase-resolved spectra; only the normalization of the power-law was different, as expected based on our selected GTIs. We also confirmed that the deviation between parameters when using a CompTT model was at the same level. Therefore, following the previous section, we froze the hydrogen column density and cutoff energy among the four spectra in order to resolve any difference in photon index arising as a function of phase. These results are displayed in Table 4. The fit statistic of the joint fit of the eight spectra (including both FPMA and FPMB data) is Cstat = 1935 for 1933 dof. We find a marginal indication of spectral variability between the two peaks ($\Gamma = 0.56 \pm 0.04$) and the soft shoulder emission ($\Gamma = 0.82 \pm 0.04$) between phase 0.0–0.25 in Figure 5. The deviation between the two photon indices is at the $\sim 3\sigma$ level.

3.3. Optical/IR Counterpart

Here, we report on our search for the counterpart of J18219 with LDT, which we supplemented with archival imaging from

PS1, ZTF, UKIDSS, and the Galactic Legacy Infrared Mid-Plane Survey Extraordinaire (GLIMPSE; Benjamin et al. 2003). At the Chandra localization of J18219, we identify a bright IR counterpart cataloged by the UKIDSS survey. The counterpart appears to be the blended combination of two point sources (star A and star B; Figure 1). In order to resolve star A and star B, we used DAOPHOT PSF photometry to deblend the sources, as outlined in Section 2.2.5. We include the archival photometry of the star A and B source complex from the GLIMPSE catalog, using the Vega to AB magnitude conversion from Papovich et al. (2016). Due to the large PSF of the Spitzer Space Telescope, we cannot deblend the photometry from GLIMPSE. However, based on the source SEDs for star A and star B, we assume that the majority of the contribution at those wavelengths (3.6–5.8 μm) is coming from star A. The photometry of both stars is tabulated in Table 1.

We did not detect an optical source coincident with the IR counterpart in our LDT and SALT imaging, or in archival PS1 and ZTF images. The 3σ upper limits at the source position are provided in Table 1. The lack of optical source detection is not unexpected given the level of interstellar reddening, $E(B - V) = 9.16$ mag (or $A_V = 28.4$ mag, assuming a ratio of total to selective extinction of $R_V = 3.1$; Rieke & Lebofsky 1985; Schlafly & Finkbeiner 2011), in the direction of the source.

Finally, we discuss here the deblended magnitudes of stars A and B (see Section 2.2.5). We show the K , $J - K$ color-magnitude diagrams for the observed field of view ($\approx 2' \times 2'$) in Figure 11 in the Vega magnitude system: stars A, B, and C are overplotted with red, blue, and green star symbols, respectively. It is interesting to note that star A is one of the reddest objects in the field of view, with $H - K \gtrsim 2.0$ mag and $J - K \gtrsim 5.0$ mag in the Vega magnitude system (not corrected for extinction). On the other hand, stars B and C are quite blue objects, with $H - K \approx 0.5$ mag (Vega) for both sources and $J - K \approx 1.5$ mag for star C and ≈ 2.0 mag for star B.

Next, we performed a comparison (using a similar methodology as Lutovinov et al. 2016) between the SEDs of star A and star B (Table 1) with the well-known BeXRBs EXO 2030+375, GX 304-1, and CEP X-4 (Coe et al. 1997; Riquelme et al. 2012; Reig et al. 2014) and with template SEDs for B0- and B2-type stars (see Figure 12). We found that a distance of 10–15 kpc is required in order for the absolute luminosity of the stars to be consistent with the expected range of values for a Be star and for a star with B0–B2 spectral class. Given this distance and the Galactic coordinates ($l, b = 17^\circ 32', 0^\circ 13'$) of the source, J18219 is likely located beyond the Galactic center, and possibly as far away as the Outer Scutum

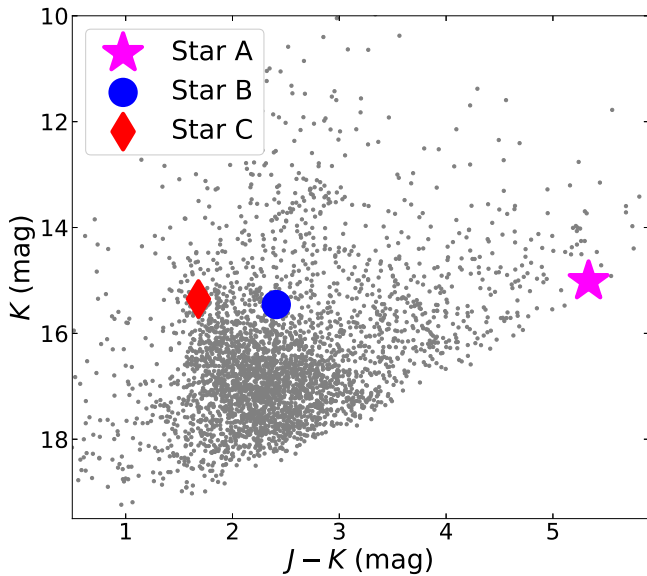


Figure 11. Color–magnitude diagrams in the Vega magnitude system for the field of J18219 based on UKIDSS IR imaging. Stars A, B, and C are represented by red, blue, and green symbols, respectively. The magnitudes are not corrected for Galactic interstellar reddening.

–Centaurus Arm of our Galaxy (Dame & Thaddeus 2011; Armentrout et al. 2017).

We find that star A is consistent with the expected SED shape of the Be- and B-type comparison stars ($J - K \approx 0$ AB mag), whereas star B is too blue in color. We note that due to the large uncertainty on the deblended J -band magnitude ($J = 21.3 \pm 0.4$ mag; not dereddened) of star A, the contribution at these wavelengths can be treated as an upper limit. For star A, we have assumed two different extinction values: (i) a Galactic extinction (see Table 1; Schlafly & Finkbeiner 2011), yielding $J - K \approx 0.3 \pm 0.4$ AB mag, and (ii) using the linear relation between hydrogen column density, N_{H} , and optical extinction, A_{V} , from Güver & Özel (2009; see their Equation (1)). In the latter case, we assumed $N_{\text{H}} = 8.3 \times 10^{22} \text{ cm}^{-2}$ (Table 2), which yields $A_{\text{V}} \sim 37.6$ mag.³² This results in $J - K \approx -0.5 \pm 0.4$ AB mag. The shaded region in Figure 12 represents the SED shape produced between these two different extinction scenarios. In either case, the SED of star A remains consistent with a Be star. We note that assuming a lower extinction value or $R_{\text{V}} < 3.1$ would imply an even redder color for the source, but would require increasing the distance to extreme values (>20 kpc).

Furthermore, we find that star C is likewise inconsistent with a Be- or B-type star due to its color ($J - K \approx -2$ AB mag) and because it is significantly brighter in the optical compared to the IR. Thus, star C is a very unlikely companion to J18219. We conclude that star A is the true counterpart to J18219, and that its Be star classification solidifies J18219 as a BeXRB.

4. Discussion

To further explore the nature of the binary system, we placed it in the Corbet diagram (Figure 13; Corbet 1986); we found that it lies solidly in the region populated by known BeXRBs

³² This conversion is computed assuming the average Galactic value of $R_{\text{V}} = 3.1$ (Savage & Mathis 1979; Rieke & Lebofsky 1985), but in principle, there is scatter in R_{V} between ~ 2 and 5.5 , allowing for more freedom in converting between N_{H} and A_{V} .

(Liu et al. 2006; Corbet et al. 2017). Additionally, it is located far away from the population of supergiant/X-ray binaries (wind-accreting systems), which generally exhibit shorter orbital periods and longer spin periods. Thus, the determination of the NS spin period, P_{spin} , is vital information in the classification of the system. We therefore argue that the location of the system near known BeXRBs, combined with the fact that the majority of its emission is over a small fraction of the orbit (Figure 3), indicates that the system is a BeXRB.

We used archival UKIDSS observations to deblend the IR counterpart into stars A and B (Figure 1), resulting in the identification of star A as a Be star (Figure 12). In addition, the source SED (and X-ray luminosity), allowed us to place it at a distance between 10 and 15 kpc. We note that at this distance, the X-ray luminosity of the observed outburst by NuSTAR is $(2\text{--}5) \times 10^{36} \text{ erg s}^{-1}$, which is toward the high end of the luminosity distribution of Type-I outbursts in HMXBs (Chaty 2011; Reig 2011). We conclude that combined with the X-ray properties, the classification of the counterpart as a Be star is compelling and confirms the nature of J18219 as a BeXRB.

Finally, a detection similar to the possible apastron outburst from J18219 (Section 3.1.1) has been observed in only a handful of other BeXRBs (e.g., EXO 2030+375; Reig et al. 1998). Reig et al. (1998) explained their apastron outburst as originating from a Be star wind with a velocity equal to or higher than the orbital velocity of the NS, leading to efficient accretion onto the NS. Alternatively, such an outburst could ensue from a possible misalignment of the binary orbit with the Be star disk. Unfortunately, the extremely limited archival X-ray data around this time period do not allow further analysis of the cause of this increase in brightness. Future monitoring of the source at apastron is required to discern whether such outbursts are regular, and to uncover their nature.

5. Conclusions

We used Swift, NuSTAR, and NICER observations to investigate the X-ray timing and spectral properties of J18219 in order to confirm the preliminary source classification as a BeXRB (La Parola et al. 2013). Through our timing analysis (Section 3.1), we uncovered a periodic signature in the NuSTAR and NICER light curves corresponding to a period $P_{\text{spin}} = 52.46$ s. We interpret this as the spin period of an NS. Furthermore, using long-term Swift/BAT daily monitoring, we confirmed the orbital period of the system $P_{\text{orb}} = 72.3 \pm 0.3$. Last, we confirmed that the IR counterpart (star A) is consistent with the expected SED of a Be star. These properties cause us to classify J18219 as a BeXRB.

We found that the time-averaged broadband X-ray spectrum (1.5–50 keV) obtained from NuSTAR and NICER was well described by either an absorbed cutoff power law (Section 3.2) with a photon index $\Gamma \sim 0.5$ and cutoff energy ~ 13 keV or a thermally Comptonized model (Table 3). The inferred hydrogen column density from our spectral modeling (Tables 2 and 3) $N_{\text{H}} = (4\text{--}11) \times 10^{22} \text{ cm}^{-2}$ is well above the Galactic value of $N_{\text{H,gal}} = 1.5 \times 10^{22} \text{ cm}^{-2}$ (Willingale et al. 2013), requiring either a significant contribution from the environment of the binary system or an excess Galactic extinction in the line of sight compared to the value implied by the 21 cm radio emission map of our Galaxy (i.e., on a scale <0.75 ; Kalberla et al. 2005; Willingale et al. 2013). Future monitoring of the source over the course of its orbit will probe whether there is

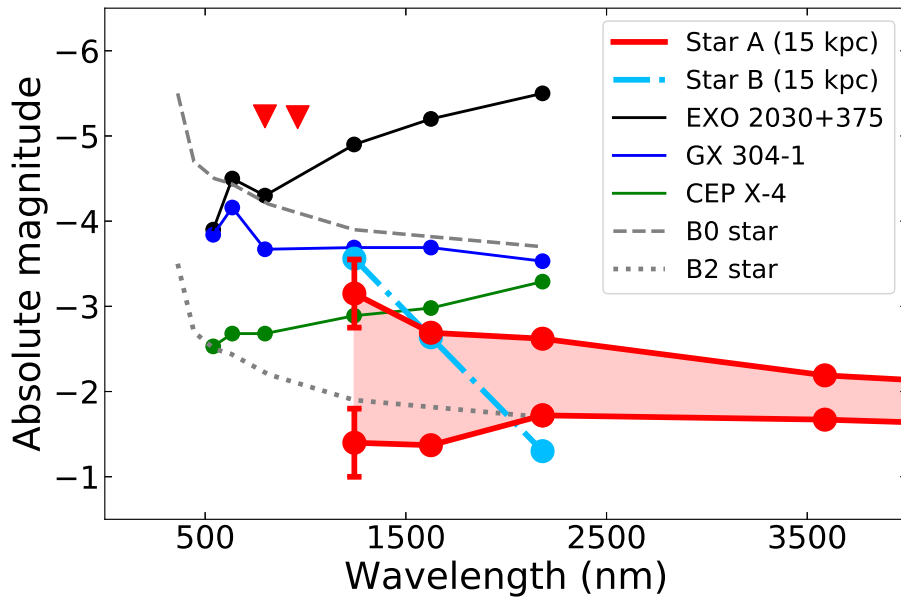


Figure 12. Absolute (AB) magnitude, assuming a distance of 15 kpc, of star A (red) and star B (light blue) vs. wavelength. Star A has been corrected for both Galactic extinction (bottom red curve; Schlafly & Finkbeiner 2011) and the expected extinction assuming $N_H = 8.3 \times 10^{22} \text{ cm}^{-2}$ (top red curve; Güver & Özel 2009); star B is only shown corrected for Galactic extinction. These stars are compared with the SEDs of known BeXRBs (EXO 2030+375, GX 304-1, and CEP X-4; Coe et al. 1997; Riquelme et al. 2012; Reig et al. 2014) that have been dereddened, as well as template SEDs for B0-type (dashed gray line) and B2-type (dotted gray line) stars. The downward red triangles represent 3σ upper limits derived from LDT and archival PS1 imaging (corrected for Galactic extinction); the limits apply for both star A and star B.

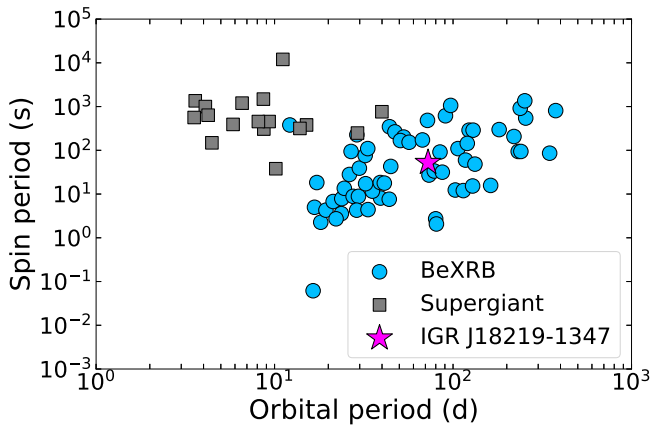


Figure 13. Corbet diagram of HMXBs with a known orbital and spin period (Liu et al. 2006; Corbet et al. 2017). Gray squares mark the location of supergiant/X-ray binary systems, and blue circles represent known BeXRBs. The location of J18219 is marked by a magenta star.

variability in the hydrogen column density, shedding light on whether the contribution is intrinsic to the source.

The authors acknowledge useful discussions with Matteo Bachetti, Tomaso Belloni, and Oleg Kargaltsev. B.O., C.K., and N.G. acknowledge supported under NASA Grants 80NSSC20K0389 and 80NSSC19K091. L.J.T. is supported by the South African National Research Foundation. J.G. acknowledges support by the ISF-NSFC joint research program (grant No. 3296/19).

This work made use of data supplied by the UK Swift Science Data Centre at the University of Leicester. This research has made use of the XRT Data Analysis Software (XRTDAS) developed under the responsibility of the ASI Science Data Center (ASDC), Italy. This research has made use

of the NuSTAR Data Analysis Software (NuSTARDAS) jointly developed by the ASI Space Science Data Center (SSDC, Italy) and the California Institute of Technology (Caltech, USA). This research has made use of data and/or software provided by the High Energy Astrophysics Science Archive Research Center (HEASARC), which is a service of the Astrophysics Science Division at NASA/GSFC. The scientific results reported in this article are based on observations made by the Chandra X-ray Observatory. This research has made use of software provided by the Chandra X-ray Center (CXC) in the application package CIAO. These results also made use of Lowell Observatory's Lowell Discovery Telescope (LDT), formerly the Discovery Channel Telescope. Lowell operates the LDT in partnership with Boston University, Northern Arizona University, the University of Maryland, and the University of Toledo. Partial support of the LDT was provided by Discovery Communications. LMI was built by Lowell Observatory using funds from the National Science Foundation (AST-1005313). Some of the observations reported in this paper were obtained with the Southern African Large Telescope (SALT) under program 2018-2-LSP-001. We additionally made use of Astropy, a community-developed core Python package for Astronomy (Astropy Collaboration et al. 2013).

Facilities: Swift, NuSTAR, NICER, SALT, LDT, UKIRT, ZTF, PS1.

Software: HEASoft v6.27.2, XRTDAS, NuSTARDAS v1.9.2, NICERDAS v7a, XSPEC v12.11.0 (Arnaud 1996), IRAF (Tody 1986), DAOPHOT (Stetson 1987), SExtractor (Bertin & Arnouts 1996), Swarp (Bertin 2010), SCAMP (Bertin 2006), astrometry.net (Lang et al. 2010), Stingray (Huppenkothen et al. 2019), Astropy (Astropy Collaboration et al. 2013).

Appendix Log of X-Ray Observations


The log of X-ray observations analyzed in this work.

Table A1
Log of X-Ray Observations of J18219, Including the Orbital Phase (Section 3.1.1) at the Time of Each Observation

Start Time (UT)	Telescope	Instrument	Exposure (s)	Orb. Phase	ObsID	References
2010-03-05 19:01:00	Swift	XRT/PC	1332	0.37	00031649001	1
2011-02-20 12:14:12	Chandra	HRC-I	1190	0.20	12499	2
2012-02-15 06:50:00	Swift	XRT/PC	1361	0.19	00032285001	1
2012-02-21 16:24:00	Swift	XRT/WT	3128	0.28	00032285002	1
2012-02-24 16:50:00	Swift	XRT/WT	3744	0.32	00032285003	1
2012-02-27 04:06:00	Swift	XRT/WT	2952	0.35	00032285004	1
2012-03-01 15:22:00	Swift	XRT/WT	1485	0.40	00032285005	1
2012-03-04 13:58:00	Swift	XRT/WT	3089	0.44	00032285006	1
2012-03-07 01:22:00	Swift	XRT/WT	3214	0.47	00032285007	1
2012-03-09 23:59:00	Swift	XRT/WT	2995	0.52	00032285008	1
2012-03-13 01:45:00	Swift	XRT/WT	3249	0.56	00032285009	1
2012-03-17 18:17:00	Swift	XRT/WT	3349	0.62	00032285010	1
2012-03-19 18:24:00	Swift	XRT/WT	2819	0.65	00032285011	1
2012-10-22 09:42:59	Swift	XRT/PC	558	0.62	00044173001	This work
2012-10-22 17:40:59	Swift	XRT/PC	461	0.62	00044172001	This work
2017-07-22 17:27:57	Swift	XRT/PC	4642	0.56	00087421001	This work
2018-02-28 11:15:57	Swift	XRT/PC	381	0.61	00087421003	This work
2020-03-05 04:03:35	Swift	XRT/PC	4512	0.76	03110746001	This work
2020-03-06 21:32:36	Swift	XRT/PC	1764	0.79	03110747001	This work
2020-03-11 12:58:36	Swift	XRT/PC	3109	0.85	03110747002	This work
2020-03-15 16:31:09	NuSTAR	FPMA/B	23000	0.91	90601309002	This work
2020-05-30 21:21:36	Swift	XRT/PC	456	0.96	03110746003	This work
2020-06-03 07:15:34	NICER	XTI	2344	0.01	3201610101	This work
2020-10-20 00:40:35	Swift	XRT/PC	4643	0.92	03110855001	This work
2021-03-09 02:22:35	Swift	XRT/PC	391	0.86	03110855002	This work
2021-05-02 11:18:40	NICER	XTI	1189	0.61	4201610101	This work

References. (1) La Parola et al. (2013), (2) Karasev et al. (2012).

ORCID iDs

B. O'Connor  <https://orcid.org/0000-0002-9700-0036>
 E. Göğüş  <https://orcid.org/0000-0002-5274-6790>
 D. Huppenkothen  <https://orcid.org/0000-0002-1169-7486>
 C. Kouveliotou  <https://orcid.org/0000-0003-1443-593X>
 N. Gorgone  <https://orcid.org/0000-0002-1653-6411>
 L. J. Townsend  <https://orcid.org/0000-0001-9788-3345>
 A. Calamida  <https://orcid.org/0000-0002-0882-7702>
 A. Fruchter  <https://orcid.org/0000-0002-6652-9279>
 D. A. H. Buckley  <https://orcid.org/0000-0002-7004-9956>
 M. G. Baring  <https://orcid.org/0000-0003-4433-1365>
 J. A. Kennea  <https://orcid.org/0000-0002-6745-4790>
 G. Younes  <https://orcid.org/0000-0002-7991-028X>
 E. Bellm  <https://orcid.org/0000-0001-8018-5348>
 S. B. Cenko  <https://orcid.org/0000-0003-1673-970X>
 K. Gendreau  <https://orcid.org/0000-0001-7115-2819>
 J. Granot  <https://orcid.org/0000-0001-8530-8941>
 C. Hailey  <https://orcid.org/0000-0002-3681-145X>
 F. Harrison  <https://orcid.org/0000-0003-2992-8024>
 D. Hartmann  <https://orcid.org/0000-0002-8028-0991>
 A. Kutuyev  <https://orcid.org/0000-0002-2715-8460>
 P. O. Slane  <https://orcid.org/0000-0002-6986-6756>
 D. Stern  <https://orcid.org/0000-0003-2686-9241>
 E. Troja  <https://orcid.org/0000-0002-1869-7817>
 A. J. van der Horst  <https://orcid.org/0000-0001-9149-6707>
 R. A. M. J. Wijers  <https://orcid.org/0000-0002-3101-1808>
 P. Woudt  <https://orcid.org/0000-0002-6896-1655>

References

- Armentrout, W. P., Anderson, L. D., Balsler, D. S., et al. 2017, *ApJ*, **841**, 121
 Arnaud, K. A. 1996, in ASP Conf. Ser. 101, *Astronomical Data Analysis Software and Systems V*, ed. G. H. Jacoby & J. Barnes (San Francisco, CA: ASP), 17
 Astropy Collaboration, Robitaille, T. P., Tollerud, E. J., et al. 2013, *A&A*, **558**, A33
 Baluev, R. V. 2008, *MNRAS*, **385**, 1279
 Barthelmy, S. D., Barbier, L. M., Cummings, J. R., et al. 2005, *SSRv*, **120**, 143
 Bellm, E. C., Kulkarni, S. R., Graham, M. J., et al. 2019, *PASP*, **131**, 018002
 Benjamin, R. A., Churchwell, E., Babler, B. L., et al. 2003, *PASP*, **115**, 953
 Bertin, E. 2006, in ASP Conf. Ser. 351, *Astronomical Data Analysis Software and Systems XV*, ed. C. Gabriel et al. (San Francisco, CA: ASP), 112
 Bertin, E. 2010, SWarp: Resampling and Co-adding FITS Images Together, *Astrophysics Source Code Library*, ascl:1010.068
 Bertin, E., & Armouts, S. 1996, *A&AS*, **117**, 393
 Buccheri, R., Bennett, K., Bignami, G. F., et al. 1983, *A&A*, **128**, 245
 Buckley, D. A. H., Swart, G. P., & Meiring, J. G. 2006, *Proc. SPIE*, **6267**, 62670Z
 Burgh, E. B., Nordsieck, K. H., Kobulnicky, H. A., et al. 2003, *Proc. SPIE*, **4841**, 1463
 Burrows, D. N., Hill, J. E., Nousek, J. A., et al. 2005, *SSRv*, **120**, 165
 Casali, M., Adamson, A., Alves de Oliveira, C., et al. 2007, *A&A*, **467**, 777
 Cash, W. 1979, *ApJ*, **228**, 939
 Chambers, K. C., Magnier, E. A., Metcalfe, N., et al. 2016, arXiv:1612.05560
 Chaty, S. 2011, in ASP Conf. Ser. 447, *Evolution of Compact Binaries*, ed. L. Schmidtbreich, M. R. Schreiber, & C. Tappert (San Francisco, CA: ASP), 29
 Coe, M. J., Buckley, D. A. H., Fabregat, J., et al. 1997, *A&AS*, **126**, 237
 Coleiro, A., & Chaty, S. 2013, *ApJ*, **764**, 185
 Corbet, R. H. D. 1984, *A&A*, **141**, 91
 Corbet, R. H. D. 1986, *MNRAS*, **220**, 1047
 Corbet, R. H. D., Coley, J. B., & Krimm, H. A. 2017, *ApJ*, **846**, 161
 Dame, T. M., & Thaddeus, P. 2011, *ApJL*, **734**, L24
 Dhillion, V. S., Marsh, T. R., Littlefair, S. P., et al. 2009, *MNRAS*, **394**, L112
 Evans, P. A., Beardmore, A. P., Page, K. L., et al. 2009, *MNRAS*, **397**, 1177
 Flewelling, H. A., Magnier, E. A., Chambers, K. C., et al. 2020, *ApJS*, **251**, 7
 Gehrels, N., Chincarini, G., Giommi, P., et al. 2004, *ApJ*, **611**, 1005
 Gendreau, K. C., Arzoumanian, Z., Adkins, P. W., et al. 2016, *Proc. SPIE*, **9905**, 99051H
 Graham, M. J., Kulkarni, S. R., Bellm, E. C., et al. 2019, *PASP*, **131**, 078001
 Grefenstette, B. W., Ludlam, R. M., Thompson, E. T., et al. 2021, *ApJ*, **909**, 30
 Güver, T., & Özel, F. 2009, *MNRAS*, **400**, 2050
 Hambly, N. C., Collins, R. S., Cross, N. J. G., et al. 2008, *MNRAS*, **384**, 637
 Harrison, F. A., Craig, W. W., Christensen, F. E., et al. 2013, *ApJ*, **770**, 103
 Hewett, P. C., Warren, S. J., Leggett, S. K., & Hodgkin, S. T. 2006, *MNRAS*, **367**, 454
 Huppenkothen, D., Bachetti, M., Stevens, A. L., et al. 2019, *ApJ*, **881**, 39
 Kalberla, P. M. W., Burton, W. B., Hartmann, D., et al. 2005, *A&A*, **440**, 775
 Karasev, D. I., Lutovinov, A. A., Revnitsev, M. G., & Krivonos, R. A. 2012, *AstL*, **38**, 629
 Kobulnicky, H. A., Nordsieck, K. H., Burgh, E. B., et al. 2003, *Proc. SPIE*, **4841**, 1634
 Krimm, H. A., Holland, S. T., Corbet, R. H. D., et al. 2013, *ApJS*, **209**, 14
 Krimm, H. A., Kennea, J. A., Holland, S. T., et al. 2012, *ATel*, **3933**, 1
 Krivonos, R., Tsygankov, S., Revnitsev, M., et al. 2010, *A&A*, **523**, A61
 La Parola, V., Cusumano, G., Segreto, A., et al. 2013, *ApJL*, **775**, L24
 Lang, D., Hogg, D. W., Mierle, K., Blanton, M., & Roweis, S. 2010, *AJ*, **139**, 1782
 Lawrence, A., Warren, S. J., Almaini, O., et al. 2007, *MNRAS*, **379**, 1599
 Leahy, D. A., Darbro, W., Elsner, R. F., et al. 1983, *ApJ*, **266**, 160
 Liu, Q. Z., van Paradijs, J., & van den Heuvel, E. P. J. 2006, *A&A*, **455**, 1165
 Lutovinov, A., & Tsygankov, S. 2008, in AIP Conf. Ser. 1054, *Cool Discs, Hot Flows: The Varying Faces of Accreting Compact Objects*, ed. M. Axelsson (Melville, NY: AIP), 191
 Lutovinov, A. A., Buckley, D. A. H., Townsend, L. J., Tsygankov, S. S., & Kennea, J. 2016, *MNRAS*, **462**, 3823
 Madsen, K. K., Grefenstette, B. W., Pike, S., et al. 2020, arXiv:2005.00569
 Masci, F. J., Laher, R. R., Rusholme, B., et al. 2019, *PASP*, **131**, 018003
 Okazaki, A. T., & Negueruela, I. 2001, *A&A*, **377**, 161
 Papovich, C., Shipley, H. V., Mehrten, N., et al. 2016, *ApJS*, **224**, 28
 Press, W. H. 1978, *ComAp*, **7**, 103
 Reig, P. 2007, *MNRAS*, **377**, 867
 Reig, P. 2011, *Ap&SS*, **332**, 1
 Reig, P., Blinov, D., Papadakis, I., Kylafis, N., & Tassis, K. 2014, *MNRAS*, **445**, 4235
 Reig, P., Stevens, J. B., Coe, M. J., & Fabregat, J. 1998, *MNRAS*, **301**, 42
 Remillard, R. A., Loewenstein, M., Steiner, J. F., et al. 2022, *ApJ*, **163**, 130
 Rieke, G. H., & Lebofsky, M. J. 1985, *ApJ*, **288**, 618
 Riquelme, M. S., Torrejón, J. M., & Negueruela, I. 2012, *A&A*, **539**, A114
 Rivinius, T., Carciofi, A. C., & Martayan, C. 2013, *A&ARv*, **21**, 69
 Savage, B. D., & Mathis, J. S. 1979, *ARA&A*, **17**, 73
 Scargle, J. D. 1982, *ApJ*, **263**, 835
 Schlafly, E. F., & Finkbeiner, D. P. 2011, *ApJ*, **737**, 103
 Smith, M. P., Nordsieck, K. H., Burgh, E. B., et al. 2006, *Proc. SPIE*, **6269**, 62692A
 Stetson, P. B. 1987, *PASP*, **99**, 191
 Stetson, P. B. 1994, *PASP*, **106**, 250
 Titarchuk, L. 1994, *ApJ*, **434**, 570
 Tody, D. 1986, *Proc. SPIE*, **627**, 733
 Toy, V. L., Cenko, S. B., Silverman, J. M., et al. 2016, *ApJ*, **818**, 79
 Willingale, R., Starling, R. L. C., Beardmore, A. P., Tanvir, N. R., & O'Brien, P. T. 2013, *MNRAS*, **431**, 394
 Wilms, J., Allen, A., & McCray, R. 2000, *ApJ*, **542**, 914